Implementing an empirical scalar tertiary anisotropic rheology (ESTAR) into large-scale ice sheet models

Felicity S. Graham[1], Mathieu Morlighem[2], Roland C. Warner[3], and Adam Treverrow[3]

[1]Institute for Marine and Antarctic Studies, University of Tasmania, Private Bag 129, Hobart, Tasmania 7001, Australia
[2]Department of Earth System Science, University of California, Irvine, California, USA
[3]Antarctic Climate and Ecosystems Cooperative Research Centre, Private Bag 80, Hobart, Tasmania 7001, Australia

Correspondence to: Felicity S. Graham (felicity.graham@utas.edu.au)

Abstract. The microstructural evolution that occurs in polycrystalline ice during deformation leads to the development of anisotropic rheological properties that are not adequately described by the most common, isotropic, ice flow relation used in large-scale ice sheet models – the Glen flow relation. We present a preliminary assessment of the implementation in the Ice Sheet System Model (ISSM) of a computationally-efficient, empirical, scalar, tertiary, anisotropic rheology (ESTAR). The effect of this anisotropic rheology on ice flow dynamics is investigated by comparing idealised simulations using ESTAR with those using the isotropic Glen flow relation, where the latter includes an overall flow enhancement factor. For an idealised embayed ice shelf, the Glen flow relation overestimates velocities by up to 17% when using an enhancement factor equivalent to the maximum value prescribed by ESTAR. Importantly, no single Glen enhancement factor can accurately capture the spatial variations in flow over the ice shelf. For flow-line studies of idealised grounded flow over varying topography or variable basal friction – both scenarios dominated at depth by bed-parallel shear – the differences between simulated velocities using ESTAR and the Glen flow relation vary according to the value of the enhancement factor used to calibrate the Glen flow relation. These results demonstrate the importance of describing the anisotropic rheology of ice in a physically realistic manner, and have implications for simulations of ice sheet evolution used to reconstruct paleo-ice sheet extent and predict future ice sheet contributions to sea level.

1 Introduction

An essential component of an ice sheet model is its formulation of ice rheology, which relates deformation rates to applied stresses. Data from laboratory ice deformation experiments can be used to define flow relations suitable for implementation in numerical ice sheet models. Previous experiments have demonstrated that under conditions of constant stress and temperature, polycrystalline ice with a statistically random distribution of crystallographic c-axes (fabric) initially behaves as a mechanically isotropic material (Budd and Jacka, 1989) where the rate of deformation is not sensitive to the character of the applied stresses. We use the term fabric to describe the distribution of crystallographic c-axis orientations within a polycrystalline aggregate. At the commencement of deformation, during the primary stage of creep, the initially high strain rate rapidly decreases. A minimum strain rate is reached during secondary creep (Fig. 1), which is associated with a transitory balance between strain hardening and the strain-induced activation of microstructural recovery processes. With continued strain, a tertiary stage of

creep is established (typically observed at strain of $\sim 10\%$ in laboratory experiments), which is characterised by a dynamic balance between microdeformation and recovery processes, statistically steady-state anisotropic polycrystalline microstructures (e.g., crystal orientation fabric and grain size), and steady strain rates that are enhanced relative to the rate observed during secondary creep.

Tertiary creep, with the associated development of polycrystalline anisotropy driven by the microstructural response to applied stresses, is the predominant mode of ice deformation in ice sheets (Budd and Jacka, 1989). The pattern of fabric anisotropy and the tertiary strain rates both depend on the nature of the applied stresses (Fig. 1). Attaining a state of tertiary creep requires that a stable pattern of stresses acts for sufficient time to develop the compatible crystal anisotropy. We can expect this tertiary state to be common throughout the bulk of a polar ice sheet from simple considerations of the observed velocities and strain rates, provided the spatial pattern of deformation varies slowly compared to the passage of ice through that pattern. Clearly there are also some regions where tertiary flow is not expected to be achieved. We discuss applicability of this tertiary creep assumption in more detail in Sects. 2.2 and 2.3, and in discussions in Sect. 6 in light of the results of the idealised experiments.

The prevailing description of ice rheology used in large-scale ice sheet models, the Glen flow relation (Glen, 1952, 1953, 1955, 1958; Nye, 1953), is a creep power law:

$$\dot{\boldsymbol{\varepsilon}} = A(T')\tau_e^{n-1}\boldsymbol{\sigma}', \tag{1}$$

where $\dot{\boldsymbol{\varepsilon}}$ is the strain rate tensor (s^{-1}), τ_e is the effective stress (Pa), proportional to the second invariant of the deviatoric stress tensor $\boldsymbol{\sigma}'$, and n is a power law stress exponent (observations support a value of $n = 3$). $A(T')$ is a flow parameter ($\mathrm{Pa}^{-n}\ \mathrm{s}^{-1}$), dependent on homologous temperature T' and persistent material properties, for which various parameterisations exist based on laboratory tests and field measurements (e.g., Budd and Jacka, 1989; Cuffey and Paterson, 2010).

The Glen flow relation was empirically derived from secondary creep rates, determined under various conditions of constant stress and temperature, for polycrystalline ice with an initially random distribution of c-axes and assuming mechanical isotropy. While the Glen flow relation captures the observed nonlinear response of ice deformation to the magnitude of applied stresses, it is unable to account for the mechanical anisotropy of polycrystalline ice that develops during the transition to tertiary creep (e.g., Nye, 1953; Glen, 1958; Budd et al., 2013). That is, it cannot explain the dependence of tertiary strain rates on the character of the applied stress. To account for the increased deformability associated with tertiary creep, a common adaptation of the Glen flow relation is the inclusion of a constant flow enhancement factor, E_G,

$$\dot{\boldsymbol{\varepsilon}} = E_G A(T')\tau_e^{n-1}\boldsymbol{\sigma}'. \tag{2}$$

The specification of E_G is typically ad hoc: E_G may be selected from reported experimental values (e.g., Duval, 1981; Jacka and Maccagnan, 1984; Pimienta et al., 1987; Treverrow et al., 2012), or used as a model tuning parameter. Such a parameter is included in most large-scale ice sheet models (e.g., Saito and Abe-Ouchi, 2004; Greve, 2005; Huybrechts et al., 2007; Winkelmann et al., 2011). Indeed, Greve and Blatter (2009) comment that it is "often introduced without explicitly mentioning anisotropy". In any case, a value of E_G that does not vary spatially in connection with the fabric and flow configuration, will

lead to an unrealistic spatial distribution of strain rates (Wang and Warner, 1999; Wang et al., 2002a; Treverrow et al., 2015). Previous studies have used anisotropic flow models or approximations to assign regional values to E_G (e.g., Ma et al., 2010) that may also vary according to the prevailing stress regime.

Budd et al. (2013) recently proposed an anisotropic flow relation based on results from laboratory ice deformation experiments involving simple shear, compression, and combinations of these. As tertiary creep rates and the corresponding compatible fabrics were found to vary according to the relative proportions of the simple shear and compression stresses, Budd et al. (2013) defined an enhancement factor E as an anisotropic function of the stress configuration, based on interpolating between separate, experimentally-determined enhancement factors for simple shear-alone and compression-alone. We refer to the generalised form of the anisotropic flow relation proposed by Budd et al. (2013) as ESTAR (Empirical, Scalar, Tertiary, Anisotropic Rheology), since it is based on tertiary (steady-state) creep rates describing the deformation of anisotropic ice and features a scalar (collinear) relationship between the strain rate and deviatoric stress tensor components.

Here, as a first step towards exploring the implications of this description of tertiary creep, we describe how to implement ESTAR in large-scale ice sheet models and apply the required changes to the Ice Sheet System Model (ISSM; Larour et al., 2012). ISSM is a thermomechanical finite element model that solves the full system of Stokes equations to describe ice flow. This will permit exploration of the ramifications of ESTAR in general ice flow situations. In an initial study here, we examine the effect of anisotropy in simple, idealised scenarios of a floating ice shelf and of grounded ice sheets, comparing simulated flow fields using ESTAR with the corresponding isotropic flow modelled by the Glen flow relation. Section 2 presents a brief overview of anisotropic rheologies, including the experimental and theoretical basis for ESTAR. Section 3 details the implementation of ESTAR in ISSM while Sect. 4 verifies the implementation against an analytical solution. In Sect. 5, we compare simulations of ice flow with ESTAR and the Glen flow relation using a suite of idealised flow geometries, including selected experiments from the Ice Sheet Model Intercomparison Project for Higher Order Models (ISMIP-HOM; Pattyn et al., 2007). Section 6 discusses the results, and implications of the ESTAR description of the flow of anisotropic ice. Conclusions are drawn together in Sect. 7.

2 Anisotropic ice rheology

A range of ice rheologies have been proposed to account for polycrystalline anisotropy. They can be broadly grouped in two categories: (1) those defined at the individual ice crystal scale, where the effects of anisotropy are parameterised based on specific properties of individual crystals, and (2) those that describe anisotropic aspects of deformation empirically: either based on regional expectations about local crystallographic microstructure, or through an empirical function of the stress configuration. In this section, we briefly review these two approaches, and the underlying experimental and modelling basis for ESTAR. In what follows, we distinguish between the Glen enhancement factor E_G and the ESTAR enhancement factor $E(\lambda_S)$, which is a function of compression deviatoric and simple shear stresses, parameterised by the shear fraction λ_S. Where necessary, we denote a more general enhancement factor, i.e., with unspecified form, as E.

2.1 Microstructure approaches

Experiments on single crystals of ice demonstrate that deformation occurs predominantly by slip on the crystallographic basal plane, with the yield stress being geometrically related to the magnitude of the applied stress resolved onto the basal plane (Trickett et al., 2000) according to Schmid's Law (Schmid and Boas, 1950). This observation, in conjunction with the development of crystallographic preferred orientations during deformation of polycrystalline ice to high strains (e.g. Russell-Head and Budd, 1979; Jacka and Maccagnan, 1984; Pimienta et al., 1987; Morgan et al., 1998; DiPrinzio et al., 2005; Durand et al., 2009; Budd et al., 2013; Montagnat et al., 2014), has driven the development of rheological descriptions in which the connection between deviatoric stresses and resulting strain-rates is regarded as an intrinsic material property determined by the effects of microstructure on bulk deformation processes, (e.g. Lile, 1978; Lliboutry, 1993; Azuma and Goto-Azuma, 1996; Staroszczyk and Gagliardini, 1999; Thorsteinsson, 2001; Gödert, 2003; Gillet-Chaulet et al., 2005; Pettit et al., 2007; Placidi et al., 2010). See also the review by Gagliardini et al. (2009). In broad terms, the anisotropic nature of these rheological descriptions is derived from the geometric relationship between the crystallographic c-axes and the stresses driving deformation, with the role of misorientation relationships between nearest neighbour grains explicitly considered in some cases.

The complexity of numerical flow relations varies according to the extent to which a physically realistic description of microdeformation and recovery processes, or a parameterisation of these, enters into the relationship between strain rates and the stresses driving deformation. Many of these rheological models are more complicated than a collinear flow relation and involve a tensor coupling in place of Eq. 2. A further consideration is the quantitative description of fabric that is used in flow relations. Those incorporating a discrete, c-axis vector based description of fabric (e.g. Lile, 1978; van der Veen and Whillans, 1994; Azuma and Goto-Azuma, 1996; Thorsteinsson, 2002) are only appropriate for highly localised studies and are incompatible with large-scale ice sheet modelling. Flow relations based on a continuous description of fabric, e.g., a parameterised orientation distribution function (ODF) or c-axis orientation tensor are also possible (e.g. Staroszczyk and Gagliardini, 1999; Gödert, 2003; Gillet-Chaulet et al., 2005; Pettit et al., 2007; Placidi et al., 2010). Including any fabric-based rheological description in an ice sheet model requires a separate set of equations governing the fabric evolution. A complication of such an approach is the computational overhead and uncertainty associated with defining the spatial distribution of fabric within ice sheets, which is poorly constrained by observations. Furthermore, for simplicity, restricted forms of the ODF or orientation tensor are specified, which may not adequately describe all fabrics likely to be encountered in an ice sheet. As such, flow relations utilising a fabric description that relies on fabric evolution equations or that is imposed as a function of location within the ice sheet are currently restricted to regional simulations (e.g., Seddik et al., 2011; Martín and Gudmundsson, 2012; Zwinger et al., 2014).

2.2 Empirical approaches

A second approach comprising experimental and observational approaches (Li et al., 1996; Wang et al., 2002a, b), modelling (Wang and Warner, 1998, 1999; Hulbe et al., 2003; Wang et al., 2003, 2004; Breuer et al., 2006; Wang et al., 2012), and theoretical studies (Warner et al., 1999), has focussed on the development and assessment of an anisotropic flow relation for

polycrystalline ice in which the nature of the crystal fabric and the magnitude of strain rate enhancement, E, are both regarded as determined by the stress regime. This assumption is supported by experimental observations for pure polycrystalline ice, which demonstrate that an accumulated strain of $\sim 10\%$ is required for the microstructure to evolve to a state that is compatible with the flow configuration, irrespective of its initial condition (Jacka and Maccagnan, 1984; Gao and Jacka, 1987; Li and Jacka, 1998; Treverrow et al., 2012). Specifically, this approach regards the fabric and the enhancement in tertiary flow as determined by the relative proportions of the simple shear and normal deviatoric stresses. For such flow relations, it is typically assumed that the spatial variation in dynamic conditions (e.g., flow configuration and temperature) only occur gradually in an ice sheet, so that the microstructure evolves to maintain compatibility with these conditions. Through most of an ice sheet we expect that the rate of microstructural evolution generally exceeds the rate at which the flow configuration varies, and that the distances travelled by a parcel of ice during the time taken to develop a compatible fabric are typically small compared to the relevant ice sheet spatial scales.

The anisotropic flow relation proposed by Budd et al. (2013) represents a continuation of this strand. They found that a scalar anisotropic flow relation, i.e., one maintaining the collinear relationship between the components of $\dot{\boldsymbol{\varepsilon}}$ and $\boldsymbol{\sigma}'$ (τ_e is a scalar function of the second invariant of $\boldsymbol{\sigma}'$) provides a good fit to laboratory data from combined compression and shear experiments. Such a scalar anisotropic rheology also simplifies the requirements for implementation within ice sheet models that are already compatible with the (scalar) Glen rheological description. Budd et al. (2013) proposed what we term ESTAR as a suitable candidate scalar anisotropic rheology generalised to arbitrary stress configurations (i.e., not restricted in its application to the limited set of experimental stress configurations described in Li et al. (1996) and Budd et al. (2013)). A simplified version of ESTAR, called ESTAR-MFL (MFL: Minimal Flow Law), has also been incorporated into the ice sheet model SICOPOLIS (SImulation COde for POlythermal Ice Sheets, http://www.sicopolis.net; Greve and Blatter, 2009, 2016).

There are of course zones within an ice sheet where the assumption of compatible tertiary flow will not apply; however, we note that these zones will be restricted in their extent. We contend that ESTAR will apply to the vast majority of the dynamically active regions of an ice sheet, in particular the zones where creep deformation makes a significant contribution to the overall flow. Specific zones where the assumption of tertiary creep may be inappropriate can be summarised as those where fabric has not yet evolved compatibility with the flow, where there is a rapid transition in the flow configuration, or where creep deformation makes only a minor contribution to the overall dynamics.

For example, in very cold ice in a low stress setting, such as the uppermost layers of the polar ice sheets, the time required to accumulate the strain necessary to develop a compatible fabric may lead to a near-surface zone in which the assumption of tertiary creep is not valid. Since the development of anisotropic fabrics provides an indication of the existence of tertiary flow, their observation at modest depths, (e.g., $\lesssim 100 - 200$ m; Morgan et al., 1997; DiPrinzio et al., 2005; Treverrow et al., 2016) allows estimation of the maximum extent of the zone where tertiary creep is not occurring. The observation within polar firn of microdeformation processes that are necessary for the development of fabric throughout ice sheets (e.g. Kipfstuhl et al., 2009; Faria et al., 2014) suggests that it may be appropriate to even further restrict the extent of the near-surface zone for which the assumption of tertiary creep is not valid. Additionally, the nonlinear nature of polycrystalline ice rheology leads to very high

viscosities in low temperature and stress environments, so that incorrectly estimating deformation rates due to the assumption of tertiary flow in such regions may be of limited importance to simulations of ice sheet evolution.

Regions where rapid transitions in dynamic conditions can lead to abrupt changes in the pattern of applied stresses and a potential breakdown in tertiary flow compatibility include ice shelf grounding zones and other locations where basal traction is lost or abruptly changes, e.g., where ice flows over a subglacial lake, or with the onset of basal sliding in ice streams. The convergence zones where tributary glaciers or ice streams merge with a larger flow unit at a high angle may also lead to a transition in dynamic conditions that is problematic for the assumption of tertiary compatibility. Of course the more highly dynamic the evolving flow regime, the more rapidly a new compatible anisotropy will be established, so that the spatial interval where the flow relations are inapplicable may be limited. While there is little guidance on how to extend empirical flow relations to parametrise ice rheology in these transition regions, we note that similar difficulties exist for a Glen-type flow relation, which unlike ESTAR does not have the benefit of being able to correctly describe anisotropic enhancement throughout the remainder of the ice sheet.

2.3 Empirical scalar tertiary anisotropic rheology (ESTAR)

Here, we summarise the anisotropic rheology proposed by Budd et al. (2013) – ESTAR – that we are implementing in ISSM as an alternative to the Glen flow relation, to provide a relation more applicable to the tertiary creep of anisotropic polycrystalline ice typical of ice sheets and glaciers. ESTAR is a scalar power law formulation based on tertiary creep rates measured in laboratory ice deformation experiments under various combinations of simple shear and compression that has been generalised to arbitrary stress configurations. Recasting Eqs. 62 and 63 of Budd et al. (2013) to more closely resemble Eq. 2, ESTAR is given by the following expression:

$$\dot{\boldsymbol{\varepsilon}} = E(\lambda_S) A(T') \tau_e^2 \boldsymbol{\sigma'}. \tag{3}$$

Assuming $n = 3$ in Eq. 2, Eq. 3 only differs from the Glen flow relation by the form of the functional enhancement factor $E(\lambda_S)$, which explicitly depends on the nature of the applied stresses via the shear fraction, λ_S, and could be regarded as providing a variable enhancement function for the Glen relation that incorporates the effect of anisotropy. We note in passing that in contrast to ISSM, flow relations in Budd et al. (2013) are couched in terms of the octahedral shear stress, $\tau_o = \sqrt{2/3}\tau_e$, which provides a more physically meaningful scalar measure of the overall stress magnitude than τ_e (Jaeger, 1969).

$E(\lambda_S)$ in Eq. 3 is defined as

$$E(\lambda_S) = E_C + (E_S - E_C)\lambda_S^2, \tag{4}$$

where E_C and E_S are the enhancement factors above the minimum or secondary deformation rate of isotropic ice under compression alone or simple shear alone, respectively. The shear fraction λ_S in Eq. 4 is a non-dimensional variable taking values in $[0, 1]$, which characterises the contribution of simple shear ($\boldsymbol{\tau'}$) to the effective stress (τ_e)

$$\lambda_S = \frac{\|\boldsymbol{\tau'}\|}{\tau_e}. \tag{5}$$

The essence of Budd et al. (2013) and ESTAR is the observation that tertiary strain rates depend on the nature of the applied stresses, and the identification of the shear fraction λ_S is the appropriate variable to characterise that pattern. Accordingly, determining the portion of the overall deformation stress that can be regarded as simple shear is the main ingredient in implementing ESTAR. This involves the identification of a particular local plane – the local non-rotating shear plane – and the determination of the shear acting on that plane, $\boldsymbol{\tau}'$, as the measure of simple shear. As discussed in Budd et al. (2013), the importance of moving beyond strain rates to consider other aspects of flow – the 'movement picture' – has been recognised since at least the 1970s (e.g., Budd, 1972; Kamb, 1973; Duval, 1981). Duval (1981) identified the plane normal to the velocity gradient in a simple shear regime as the 'permanent shear plane' and discussed its role in the evolution of crystal fabrics. Budd et al. (2013) proposed a definition for this local plane in an arbitrary flow as the plane containing the vorticity vector associated solely with deformation and the velocity vector. As discussed below they also prescribed a further projection to remove any component of $\boldsymbol{\tau}'$ parallel to the deformational vorticity. The collinear nature of ESTAR (Eq. 3) allows λ_S to be written in terms of the corresponding strain rates, which is more convenient for Stokes flow modelling, as

$$\lambda_S = \frac{\dot{\varepsilon}'}{\dot{\varepsilon}_e}, \tag{6}$$

where $\dot{\varepsilon}'$ is the magnitude of the shear strain rate on the locally non-rotating shear plane, as defined in Eq. 7 below. In compression-alone scenarios, including three-dimensional uniaxial compression and two-dimensional plane compression and extension, $\lambda_S = 0$, so that $E(\lambda_S) = E_C$. Similarly, for simple shear alone, $\lambda_S = 1$ and $E(\lambda_S) = E_S$.

Analysis of tertiary creep rates for experiments conducted in simple shear-alone and compression-alone suggests that a suitable ratio of E_S to E_C for ice sheets is $\sim 8/3$ (Treverrow et al., 2012). The same study also suggests that $E \propto \sqrt{\tau_e}$ for tertiary creep rates determined over a range of stress magnitudes. A flow relation incorporating such a stress dependent enhancement could be achieved by employing a creep power-law stress exponent of $n = 3.5$, rather than the more commonly used $n = 3$, assuming both E_S and E_C are described by functions of $\sqrt{\tau_e}$. For simplicity, we have excluded the apparent stress dependence of E_S and E_C in our initial implementation of ESTAR in ISSM since further work is required to verify the stress dependence of E_S and E_C experimentally for complex, combined stress configurations. Accordingly, we use scalar enhancement factors of $E_S = 8$ and $E_C = 3$ for the idealised scenarios examined in this study. These values may be at the higher end of the anticipated range in E_S and E_C for an ice sheet (see e.g., Russell-Head and Budd, 1979). However, the strength of anisotropy and its influence on ice dynamics in comparison to the enhanced Glen flow relation depends on the ratio E_S/E_C and its spatial variation, i.e., the dynamically controlled distribution of $E(\lambda_S)$.

If the enhancement parameters are selected so that $E_C = E_S = E_G$, where E_G is the Glen enhancement factor, ESTAR becomes isotropic and equivalent to the Glen flow relation since $E(\lambda_S) \equiv E_G$. However, the viscous creep behaviour of polycrystalline ice is highly anisotropic and regional variations in the relative proportions of shear and normal strain rates, which are driven by variations in the distribution of the stresses responsible for deformation, mean that spatial contrasts in anisotropy are common and widespread in ice sheets. For this reason, a spatially varying enhancement factor is required for ice sheet modelling (e.g., Morgan et al., 1998; Wang and Warner, 1999; Wang et al., 2002a).

Comparisons of simulations of ice sheet dynamics using ESTAR and the Glen flow relation will be influenced by: the choice of the Glen enhancement parameter, E_G; the ESTAR parameters E_C and E_S; and the spatial distribution of λ_S. The most significant differences between Glen- and ESTAR-based simulations are expected where there are regional contrasts in λ_S. Specific regions where these conditions are likely to arise include: the progression with increasing depth in the ice sheet from a regime of normal stresses to one dominated by bed parallel shear; the contrasts between lateral margins of embayed ice shelves and ice streams and their central flows; and where there is significant relief in the bedrock topography.

A caveat is that as stated earlier, for ESTAR the assumptions of crystallography and deformation rates being compatible with the instantaneous stress/deformation regime requires that this does not change too rapidly along the flow. That is to say, for a compatible (tertiary) anisotropy to be present, the present deformation regime needs to be a suitable indicator of the recent strain history of the flowing ice.

3 Implementation of ESTAR

The magnitude of the shear strain rate defined on the local non-rotating shear plane, $\dot{\varepsilon}'$ for Eq. 6, is central to the formulation of ESTAR (Eqs. 3-4). The full prescription, following Budd et al. (2013), involves the expression

$$\dot{\varepsilon}' = \|\dot{\boldsymbol{\varepsilon}} \cdot \mathbf{n} - (\mathbf{n} \cdot (\dot{\boldsymbol{\varepsilon}} \cdot \mathbf{n}))\,\mathbf{n} - (\hat{\boldsymbol{\omega}}_D \cdot (\dot{\boldsymbol{\varepsilon}} \cdot \mathbf{n}))\,\hat{\boldsymbol{\omega}}_D\|, \tag{7}$$

where: $\mathbf{n}$ is the unit normal to the non-rotating shear plane, $\hat{\boldsymbol{\omega}}_D$ is the unit vector parallel to that part of the vorticity that is associated solely with deformation ($\boldsymbol{\omega}_D$), and $\dot{\boldsymbol{\varepsilon}}$ is the strain rate tensor. The unit normal to the non-rotating shear plane, $\mathbf{n}$, is defined as the normalised cross product of the velocity and the deformational vorticity

$$\mathbf{n} = \frac{\mathbf{v} \times \boldsymbol{\omega}_D}{\|\mathbf{v} \times \boldsymbol{\omega}_D\|}. \tag{8}$$

The last projection term in Eq. 7 was proposed in Budd et al. (2013) to prevent any shear component parallel to the deformational vorticity from contributing to the measure of simple shear.

The vorticity of a flow, whether viewed as the anti-symmetrised part of the velocity gradient tensor or as the usual vector $\boldsymbol{\omega} = \nabla \times \mathbf{v}$, contains motions associated with both deformation and local rigid-body rotation. The locally non-rotating shear plane is intended to be rotating with any rigid rotation portion of the flow field, so it is only vorticity associated with the deformation process that is relevant to determining the shear fraction. Accordingly we formally decompose vorticity into deformational and rotational parts:

$$\boldsymbol{\omega} = \nabla \times \mathbf{v} = \boldsymbol{\omega}_D + \boldsymbol{\omega}_R. \tag{9}$$

For the present implementation it is convenient to decompose the vorticity further, into vectors perpendicular and parallel to the velocity direction as follows:

$$\boldsymbol{\omega} = \boldsymbol{\omega}_D^{\perp} + \boldsymbol{\omega}_R^{\perp} + \boldsymbol{\omega}_D^{\parallel} + \boldsymbol{\omega}_R^{\parallel}. \tag{10}$$

From Eq. 8, only the perpendicular projection $\boldsymbol{\omega}_D^{\perp}$ of the deformational vorticity is relevant in determining the direction of the normal to the non-rotating shear plane. This is fortunate since the perpendicular projection of the rotational vorticity can be calculated directly for steady flow from the flow speed and the curvature of the local flowline, and is oriented along the bi-normal to the flow-line. The decomposition of the component of vorticity parallel to the flow direction, conventionally termed swirling motion, into deformational and rotational pieces is not so straightforward, but we can use the following expression, which can be calculated using variables available within an individual element of ISSM to generate a vector suitable for computing $\mathbf{n}$:

$$\tilde{\boldsymbol{\omega}}_D = \nabla \times \mathbf{v} - \frac{2\mathbf{v} \times ((\mathbf{v} \cdot \nabla)\mathbf{v})}{\|\mathbf{v}\|^2}. \tag{11}$$

This vector contains the correct perpendicular component $\boldsymbol{\omega}_D^{\perp}$ to compute $\mathbf{n}$ using Eq. 8, but contains all of $\boldsymbol{\omega}_D^{\parallel} + \boldsymbol{\omega}_R^{\parallel}$. We can obviously also project out the component parallel to velocity to find

$$\boldsymbol{\omega}_D^{\perp} = \tilde{\boldsymbol{\omega}}_D - (\mathbf{v} \cdot \tilde{\boldsymbol{\omega}}_D)\frac{\mathbf{v}}{\|\mathbf{v}\|^2}. \tag{12}$$

In the present implementation of ESTAR, we assume that swirling effects are small for flows with the relevant spatial scales, aspect ratios etc., which can be verified from the modelled flow-fields in our test cases, and hence $\boldsymbol{\omega}_D^{\parallel}$ is also expected to be small. We use the unit vector corresponding to $\boldsymbol{\omega}_D^{\perp}$ (i.e., $\hat{\boldsymbol{\omega}}_D$) in Eq. 7 for our computation of $\dot{\varepsilon}'$. This corresponds to extracting the component of the shear resolved on the non-rotating shear plane which is parallel to the velocity direction, which could be regarded as an alternative generalisation for the simple shear to that proposed by Budd et al. (2013). No approximation is involved for flows that are exactly two dimensional in character, since vorticity is always orthogonal to velocity in such situations.

The ESTAR description above is implemented in ISSM for the full-Stokes (FS) model of flow. We also extended the implementation of ESTAR to ISSM versions of the higher-order (HO) three-dimensional model of Blatter (1995) and Pattyn (2003), and the shallow-shelf approximation (SSA) of MacAyeal (1989). The HO model is derived from the FS model by assuming that horizontal gradients in the vertical velocities are negligible ($\partial v_z/\partial x << \partial v_x/\partial z$ and $\partial v_z/\partial y << \partial v_y/\partial z$) compared with vertical gradients in the horizontal velocities, and longitudinal derivatives of vertical shear stress (bridging effects van der Veen and Whillans, 1989) are ignored. The HO vertical velocities are recovered directly through incompressibility. Extending on the HO model assumptions, for the SSA model, vertical shear is assumed to be negligible ($\dot{\varepsilon}_{xz} = \dot{\varepsilon}_{yz} = 0$). For both the HO and SSA models, the approximations will affect calculations of the total vorticity and hence the magnitude of the shear strain rate on the non-rotating shear plane (Eq. 7) and λ_S (Eq. 6).

4 Analytical verification

We perform convergence tests in order to verify the implementation of ESTAR within the ISSM FS and HO models. The objective of these tests is to compare the model results to analytical solutions for different mesh resolutions. As the mesh becomes finer, the error between the model and the analytical solution (i.e., $\sqrt{\int_\Omega (X - X_\mathrm{a})^2 / \int_\Omega X_\mathrm{a}^2}$, for model solution X,

analytical solution X_a, and domain Ω) should decrease, with a cubic dependence on resolution for FS (quadratic for ice pressure) when using Taylor-Hood finite elements, and a quadratic dependence for HO using P1×P1 finite elements (e.g., Ern and Guermond, 2004).

We designed our analytical solutions by considering a three-dimensional, grounded, isothermal ice slab of unit dimension lying on a flat bed topography, with cartesian coordinates (x, y, z), where z is vertically upward and where there is no gravitational force. The FS three-dimensional velocity field is given by

$$v_x(x, y, z) = 3z, \tag{13}$$

$$v_y(x, y, z) = 2x + y, \tag{14}$$

$$v_z(x, y, z) = -z, \tag{15}$$

and the HO velocity field by

$$v_x(x, y, z) = x^2, \tag{16}$$

$$v_y(x, y, z) = 3z + y. \tag{17}$$

In the case of the HO model, $v_z(x, y, z)$ is recovered by incompressibility. For both FS and HO models, we use ESTAR shear and compression enhancement factors of $E_S = 3$ and $E_C = 1$, and the flow parameter $A(T') = 2/3$ Pa^{-3} s^{-1}. The open source mathematics software system SageMath (http://www.sagemath.org/) is used to calculate analytical solutions for the force balance equations based on the above velocity fields:

$$f_x(x, y, z) = -\left(\frac{\partial \sigma'_{xx}}{\partial x} + \frac{\partial \sigma_{xy}}{\partial y} + \frac{\partial \sigma_{xz}}{\partial z}\right), \tag{18}$$

$$f_y(x, y, z) = -\left(\frac{\partial \sigma_{xy}}{\partial x} + \frac{\partial \sigma'_{yy}}{\partial y} + \frac{\partial \sigma_{yz}}{\partial z}\right), \tag{19}$$

$$f_z(x, y, z) = -\left(\frac{\partial \sigma_{xz}}{\partial x} + \frac{\partial \sigma_{yz}}{\partial y} + \frac{\partial \sigma'_{zz}}{\partial z}\right). \tag{20}$$

Here, the deviatoric stress fields are calculated using ESTAR as specified in Eq. 3. When the total, rather than deformational, vorticity (i.e., without inclusion of the rigid body correction or removal of the vorticity component aligned with the flow) is used in the calculation of ESTAR, the FS analytical solution for (f_x, f_y, f_z) comprises (20 521, 9 190, 20 523) characters. By contrast, non-trivial analytical solutions for the forcing functions that are calculated from an anisotropic enhancement factor that is based on the deformational, rather than total, vorticity are at minimum 200 000 characters, well in excess of the character limits for most compilers. Accordingly, we verify ESTAR using the total, rather than the deformational, vorticity.

To test the numerical implementation of ESTAR, ISSM is forced using the analytical expressions for f_x, f_y, and f_z in Eqs. 18-20 and the resulting three-dimensional flow field is compared with the relevant analytical specification in Eqs. 13-17. Since the aim is to verify correct coding of the ESTAR modifications within ISSM, we apply the analytic velocities on the faces as the boundary conditions. Four sets of element sizes are used for each of the FS and HO models, increasing in resolution from 0.2 (272 elements over 5 vertical layers) to 0.08 (4656 elements over 13 vertical layers). We find convergence powers of

2.5 (v_x), 3.1 (v_y), and 2.6 (v_z) for FS, respectively, and 1.4 (v_x) and 1.1 (v_y) for HO (Fig. 2), which are consistent with theory and verify our implementation.

5 Application of ESTAR to idealised scenarios

ESTAR was applied to a suite of test cases. The first case we present simulates flow in an embayed ice shelf; the second two are based on experiments from the Ice Sheet Model Intercomparison Project for Higher Order Models (ISMIP-HOM; Pattyn et al., 2007). The ISMIP-HOM experiments describe idealised scenarios of ice flow where the bed topography or basal friction vary. ISSM has already been validated against the ISMIP-HOM experiments (Larour et al., 2012).

In each experiment, the velocity, surface, and thickness fields were allowed to run to steady-state, as defined in the corresponding section below (the original ISMIP-HOM experiments were simply diagnostic). The ice sheet is isothermal in each case.

As mentioned above, we use ESTAR shear and compression enhancement factors of $E_S = 8$ and $E_C = 3$, respectively (Treverrow et al., 2012). For each experiment, we performed simulations using a range of Glen enhancement factors (1, 3, 5, and 8), but since these idealised experimental systems have simple scaling properties under global changes in flow rates, we present only results for $E_G = 8$ since that proved the most directly relevant value. The ISMIP-HOM experiments used the original parameter values (Pattyn et al., 2007) unless otherwise indicated.

5.1 Flow through an embayed ice shelf

The first experiment simulates three-dimensional flow through a rectangular embayed ice shelf. The experiment was carried out for model domains with transverse spans $x \in [0, L]$, for $L = 20$, 60, and 100 km and along-flow dimension $y \in [0, 100]$ km. The initial ice thickness decreases uniformly from 1000 m at the grounded zone to 300, 600, and 850 m at the ice front for the $L = 20$, 60, and 100 km cases, respectively. The main features of the anisotropic effects are similar regardless of aspect ratio. This is principally because wider embayed ice shelves are flatter so that the influence of simple shear stresses on the dynamics is not particularly sensitive to aspect ratio. Accordingly, we focus our discussion on one transverse length scale: $L = 20$ km. The plan view mesh is extruded ten quadratically-spaced layers in the vertical. A no-slip boundary condition is applied along the $x = 0$ and $x = L$ side boundaries. At the inflow boundary, the y-component of velocity is set to

$$v_y(x, 0) = V_0 e^{-\left[\frac{5(x - x_{\mathrm{mid}})}{2L}\right]^8}, \tag{21}$$

where $V_0 = 100\ \mathrm{m\ yr^{-1}}$ and $x_{\mathrm{mid}} = L/2$. As is standard, ocean water pressure is applied at the ice-ocean interface where tangential (traction) stresses vanish. It is assumed that there is no surface or basal melting or accumulation over the ice shelf domain. The flow parameter $A(T') = 1.74 \times 10^{-25}$ $\mathrm{Pa^{-3}\ s^{-1}}$, is set using the Budd and Jacka (1989) value for an isothermal ice shelf of -20 °C. We consider the case where the Glen enhancement factor is equal to the ESTAR shear enhancement factor, i.e., $E_G = E_S = 8$.

We run the HO ice flow model for each of the ESTAR and Glen rheologies to steady-state, which we define to be reached when the mean velocity change over the surface mesh points is less than 1×10^{-2} m yr^{-1} between two consecutive time steps (of $\triangle t = 2$ yr).

The Glen and ESTAR HO steady-state surface velocity magnitudes are compared in Fig. 3. The patterns of ice flow are similar for the two rheologies: in each case the ice velocity increases as it flows through the ice shelf, reaching its maximum at the ice front. Over most of the domain the velocities are in close agreement, reflecting the dominance of the shear flow. However, the Glen velocities are up to 17% larger than the ESTAR velocities at the ice front, where the flow field is predominantly extensive in accordance with the ice front boundary conditions. The differences in velocities can be attributed to differences in flow enhancement factors for simple shear and compression. Near the centre line of the ice shelf and across the ice front, where longitudinal and vertical normal stresses dominate, the Glen enhancement is as much as $8/3$ times larger than the corresponding ESTAR enhancement.

The steady-state thickness ratio for the two rheologies is shown in Fig. 3d. In both cases, the equilibrated ice shelf is thicker along the centre line and thinner towards the side margins where ice flow is slower, and thicknesses agree within 5% over much of the domain. However, the Glen ice shelf is consistently thinner than the ESTAR ice shelf, particularly along the centre line where Glen velocity is enhanced relative to ESTAR, and it is up to 20% thinner at the ice front.

The ESTAR strain rate components are presented in Fig. 4. As expected, shear strain rate in the $x-y$ plane is very high near the lateral boundaries (Fig. 4d). However, it dominates the effective strain rate (and hence λ_S) well beyond those margins (Fig. 5), before decreasing towards the centre line, where it identically vanishes. Towards the ice-ocean front, each of the normal strain rates – $\dot{\varepsilon}_{xx}$, $\dot{\varepsilon}_{yy}$, and $\dot{\varepsilon}_{zz}$ – increase in magnitude, reaching their maxima at the front. The (approximately) longitudinal $\dot{\varepsilon}_{yy}$ is the dominant normal strain rate component and is extensive towards the front. Due to the confined geometry, towards the front $\dot{\varepsilon}_{yy}$ is largely balanced by $\dot{\varepsilon}_{zz}$, which drives ice shelf thinning. Transverse normal strain rate $\dot{\varepsilon}_{xx}$ plays a lesser role at the ice-ocean front than the other normal strain rates. It is extensive along the front as the streamlines diverge, but changes sign to compressive towards the corners. The patterns in the component strain rates, including the dominance of normal strain rates in the centre of the ice shelf and at the ice-ocean front, are evident in the strain rate on the non-rotating shear plane ($\dot{\varepsilon}'$) and the effective strain rate ($\dot{\varepsilon}_e$), the ratio of which sets the magnitude of λ_S (Fig. 5). In the ESTAR embayed ice shelf simulation, the vanishing of basal traction and the depth independent nature of the inflow velocity lead to an almost 2D flow field with local non-rotating shear planes essentially vertical where they can be defined – there being neither $x-y$ plane shear nor vorticity along the centre line. We note that $\dot{\varepsilon}_{yy}$ decreases in magnitude with depth at the ice-ocean front, coincident with ice front tilting (Weertman, 1957), which also gives rise to some local shear deformation in the $y-z$ plane.

To assess the computational demands of the full ISSM model with ESTAR, the FS ice flow model was computed for one model year (i.e., steady state had not yet been reached) and the results compared with the HO simulation results for the same model period (results not shown). At the ice front, the HO velocities are everywhere within 5% of the FS velocities, with the maximum differences occurring near the lateral boundaries. Across the shelf, the HO component velocities accord well with the FS velocities. The magnitude and spatial patterns of $\dot{\varepsilon}'$, $\dot{\varepsilon}_e$, and λ_S also agree well between the FS and HO models.

Computation times for FS simulations using each of the two rheologies, and for increasing mesh resolutions, are summarised in Table 1. In each case, the model was run for 1 month with a time step of $\triangle t = 1 \times 10^{-4}$ yr. The ESTAR simulation computation times are no more than 3% slower than the corresponding Glen times, and the simulation times for the two rheologies converge as the mesh resolution increases. This result gives us confidence that ESTAR is essentially as computationally-efficient as the Glen rheology.

5.2 ISMIP-HOM experiment B: two-dimensional flow over a bumpy bed

ISMIP-HOM Experiment B (ISMIPB) describes two-dimensional flow (x horizontal, z vertical) over a bed topography that varies sinusoidally, according to the following equation

$$z_b(x) = z_s(x) - 1000 + 500 \sin\left(\frac{2\pi x}{L}\right). \tag{22}$$

where $z_s(x) = -x \tan\alpha$, for a mean bed slope of $\alpha = 0.5°$, and L controls the scale of the bedrock undulation. We take $z_s(x)$ as the initial surface so that the mean initial ice thickness is 1000 m. We present results for two different aspect ratios, $L = 20$ km and $L = 5$ km, to explore the influence of different longitudinal stresses. In each case we used the full-Stokes (FS) version of ISSM. The flow parameter is fixed at 3.96×10^{-25} Pa^{-3} s^{-1}, corresponding to an ice temperature of approximately $-14°$ C (Budd and Jacka, 1989). The value for the flow parameter in the original ISMIPB was 3.17×10^{-24} Pa^{-3} s^{-1}, which corresponds to a Budd and Jacka (1989) ice temperature of approximately $-3.6°$ C. We have reduced the original flow parameter by a factor of 8 (i.e., equal to E_S) to ensure our results are as close as possible to the original ISMIP-HOM experiments. Periodic boundary conditions are applied at the vertical edges of the domain and a no-slip boundary condition is applied at the base. In this and the following two-dimensional test case, the normal to the non-rotating shear plane is simply the direction perpendicular to the velocity and there is no uncertainty about the vorticity (which has only one non-vanishing component) being perpendicular to the velocity. Steady-state is regarded as reached when the mean velocity change over the surface mesh points is less than 1×10^{-2} m yr^{-1} between two consecutive time steps of $\triangle t = 1$ yr for this and the following ISMIP-HOM experiment.

In what follows, we consider the case when the Glen enhancement factor is equal to the ESTAR shear enhancement factor, i.e., $E_G = E_S = 8$. This is the most relevant case for the ISMIPB experiment as the dynamics here are driven by bed-parallel shear, as discussed below.

The ESTAR and Glen FS steady-state horizontal velocities (v_x) for ISMIPB for $L = 20$ km are shown in Fig. 6a and b, with their ratio in Fig. 6c. The shear fraction (λ_S) used to calculate the ESTAR enhancement is shown in Fig. 6d. The ESTAR velocities are marginally slower than the Glen velocities throughout the domain, regionally by as much as 6%. While in a real-world situation, a local difference of 6% may not be significant to overall flow, clearly unless the Glen enhancement factor is approximately E_S there would be a significant and widespread difference in velocities. One major contrast occurs either side of the topographic bump in the near-surface layers (Fig. 6c) where normal stresses dominate ($\lambda_S < 1$; Fig. 6d) and $E(\lambda_S)$ tends to $E_C < E_G$, as λ_S tends to 0. This reduces the shear deformation in the upper-layers for ESTAR compared to Glen, leading to slightly lower horizontal velocities near the surface. We will discuss the relevance of this in Sect. 6. Another major

velocity contrast occurs in the lowest part of the ice sheet directly above the topographic depression. Since deformation here is clearly shear dominated ($\lambda_S = 1$ for essentially the whole column), the differences must arise from a varying but consistently lower shear stress profile in the ESTAR case, reflecting indirectly the distributed effect of the stiffer ice in the upper layers where $E(\lambda_S) < E_G$ and a slightly different final geometry of the ice surface. In contrast, the closest agreement between the two velocity distributions is in the basal region over the topographic high.

Figure 6 also shows the FS $\dot{\varepsilon}_{xz}$ and $\dot{\varepsilon}_{xx}$ strain rates for the ESTAR simulation: effectively the shear and normal strain rates. The dominance of high values of λ_S indicates that bed-parallel simple shear is the main driver of ice flow in ISMIPB with the expected transition through the ice column from compression/extension-dominated flow near the surface to shear-dominated flow near the non-slip bed. Note that while the component strain rates are presented in the background cartesian frame, λ_S denotes the relative importance of simple shear on local non-rotating shear planes. Peaks in λ_S appear directly over the topographical bump and depression, extending further into the surface layers than in surrounding regions. The locations of the peaks in λ_S correspond to the transitions between extensive and compressive longitudinal stresses, centred on "transition curves" (Fig. 6e), along which normal strain rates are identically zero.

In addition to the case where $L = 20$ km, we also investigated the impact of reducing the horizontal extent to $L = 5$ km. In this steeper bed scenario (Fig. 7), the ESTAR surface velocities are at least 11% slower than the Glen velocities in the surface layers across the whole domain, as much as 20% slower around the topographic bump, and up to 25% slower in the topographic depression (Fig. 7c). The much greater reductions in the magnitude of the ESTAR velocities for $L = 5$ km are a consequence of the increasing importance of longitudinal stresses in the stress balance equations for the smaller aspect ratio (Fig. 7e), and also in some areas the lower strain rates, which lead to correspondingly stiffer ice. Indeed we see a clear decline in the shear strain rate in the lower part of the bed depression in Fig. 7f, in contrast to Fig. 6f. The qualitative pattern of the longitudinal strain-rates in Fig. 7e is similar to the $L = 20$ km case, although the horizontal gradients are naturally accentuated, and the "transition curves" are displaced.

In order to examine the dynamics giving rise to the high shear-dominance peaks in Fig. 6d and Fig. 7d, we consider the following exact form of λ_S^2 (for these two-dimensional flow fields) expressible using the cartesian frame strain rate components

$$\lambda_S^2 = \frac{\alpha\dot{\varepsilon}_{xx}^2 + \beta\dot{\varepsilon}_{xz}^2 + \gamma\dot{\varepsilon}_{xx}\dot{\varepsilon}_{xz}}{\dot{\varepsilon}_{xx}^2 + \dot{\varepsilon}_{xz}^2}, \tag{23}$$

for some spatially varying coefficients α, β, and γ. Since there is no surface accumulation, velocities and hence local non-rotating shear planes at the ice sheet surface are parallel to the surface. The traction free surface boundary condition implies that the numerator ($\dot{\varepsilon}'^2$) in Eq. 23, and accordingly λ_S, vanishes at the surface, except that if $\dot{\varepsilon}_e$ also vanishes, λ_S is technically undefined. Our implementation sets $\lambda_S = 0$ for vanishing $\dot{\varepsilon}'$ in such situations. It is apparent from Eq. 23 that along the transition curves, i.e., where $\dot{\varepsilon}_{xx} = \dot{\varepsilon}_{zz} = 0$, $\lambda_S^2 = \beta$, independent of (non-zero) $\dot{\varepsilon}_{xz}$ strain rate. One can show that $\beta \to (1 - S_x^2)^2$ towards the surface (i.e., for surface slope in the x-direction S_x) along the transition curve, in order to satisfy the surface boundary condition. This indicates that λ_S would be finite along the transition curves all the way to the surface, except that

we enforced its vanishing there. For these locations, the Glen and ESTAR viscosities corresponding to Eqs. 2-3 would tend to infinity as $\dot{\varepsilon}_e$ vanished approaching the surface, but are limited to a maximum value in the ISSM implementation.

Note that away from the transition curves λ_S goes to zero as we approach the surface, associated with vanishing shear on the non-rotating shear plane and the corresponding dominance of normal deformations. We return to these near-surface spikes in λ_S in the discussion.

5.3 ISMIP-HOM experiment D: two-dimensional flow over a sticky spot

ISMIP-HOM experiment D (ISMIPD) describes a two-dimensional domain over which the basal friction coefficient χ varies sinusoidally in the horizontal direction. A Paterson-type friction law (Paterson, 1994) of the following form is used

$$\tau_b = -\chi^2 v_b, \tag{24}$$

where τ_b is the basal stress and v_b the basal velocity, and the friction coefficient, χ^2 (Pa a m^{-1}), varies according to the equation

$$\chi^2 = 1000 + 1000 \sin\left(\frac{2\pi}{L}x\right). \tag{25}$$

The bed topography and the initial ice surface are inclined planes with a slope of $0.1°$, and the initial thickness is 1000 m throughout the domain. As in the preceding ISMIPB experiments, the flow parameter is taken as $A(T') = 3.96 \times 10^{-25}$ Pa^{-3} s^{-1} (the ISMIPB and ISMIPD original flow parameters were equal). Periodic boundary conditions are applied at the edges of the domain. Once again, we present results for steady-state solutions for two different horizontal scales: $L = 20$ km and $L = 5$ km. As with the ISMIPB experiments above, we employ the full-Stokes (FS) solver in ISSM. Consistent with ISMIPB, the control of the final deformation flow in the ISMIPD experiment is bed-parallel shear, so we consider the case when the Glen enhancement factor is equal to the ESTAR shear enhancement factor, i.e., $E_G = E_S = 8$.

The Glen and ESTAR FS results for ISMIPD when $L = 20$ km are shown in Fig. 8. For both rheologies, the fastest velocities develop in the upper part of the column over the sticky spot (centred around 5 km). This is required by continuity, given the lower basal velocities over the sticky spot, to balance the block flow over the slippery section (basal friction coefficient vanishes at 15 km). The basal velocities increase as the basal friction coefficient decreases. The total steady-state ESTAR velocities are everywhere within 1% of the corresponding Glen velocities (see Fig. 8c), with the maximum difference occurring in the near-surface layers over the sticky spot, where the ESTAR ice is stiffer, as shown by the corresponding contrast in viscosities (Fig. 8e). Sliding occurs throughout the domain and the deviations from block flow are modest throughout, so to explore what differences might be associated with the departure from block flow we calculated "deformational velocities" from v_x by subtracting the basal motion, and examined the ratio between ESTAR and Glen cases (Fig. 8d). The most notable feature of this ratio is a localised 50% decrease in deformational velocity for ESTAR compared to Glen through the entire column, peaking directly over the point where the basal friction coefficient (Eq. 25) vanishes. This major band of difference coincides with the band of higher viscosity for ESTAR, relative to Glen, (see Fig. 8e) over the slippery region.

The ESTAR component strain rates and shear fraction λ_S are illustrated in Fig. 9 for ISMIPD, for the $L = 20$ km case. The plot of λ_S (Fig. 9d) depicts transitions in the deformation regime from shear-dominated to compression/extension-dominated

and back over a few kilometres around the slippery spot. These transitions extend all the way to the bed, becoming perpendicular to the ice flow direction and reflect the low shear over the slippery region. This is in marked contrast to the ISMIPB experiments, where the shear deformation regime dominated except near the free surface. We discuss the implications of these abrupt transitions for the assumptions that underpin ESTAR in the next section. Shear dominates much of the ice column ($\lambda_S > 0.5$) throughout the rest of the domain (over the region where values of the basal friction coefficient exceed 10% of the maximum value). The shear strain rates are greatest in the region of maximum stickiness at approximately 5 km, and a steep profile in the shear strain rate is present there. Naturally, transitions between extensive and compressive flows occur around the sticky spot and the transition curves (vanishing normal strain rates) resemble the ISMIPB cases (Fig. 6e). Here the transition curves reach the surface as the friction coefficient increases, and just downstream of its peak value (the sticky spot), leading to near surface spikes of high values λ_S analogous to ISMIPB. It should be noted that the strain rates here are very small compared to the ISMIPB experiments. The viscosity ratio in Fig. 8e reveals that there are also lower strain rates for ESTAR in the compression dominated regions, as the ratios there are higher than the factor of 1.39 that would be produced by the influence of $E(\lambda_S)$ alone.

The results of a FS prognostic run to steady-state for the ISMIPD experiment for $L = 5$ km are presented in Fig. 10. The v_x velocity ratio (Fig. 10c) shows that very little difference is seen between results for the two flow relations, unlike the ISMIPB experiments in the previous section, where differences up to 25% between ESTAR and Glen cases emerged for the shorter bedrock periodicity. The tiny differences in overall velocities are enhanced but the patterns in Fig. 8c and Fig. 10c are similar. However, there is a significantly different picture in the ratio of deformation velocities seen in Fig. 10d, compared to Fig. 8e. The largest differences are now limited to the lower portion of the ice column and for much of the region over the slippery bed the ratio is almost unity.

The pattern of deformation regimes mapped by λ_S (Fig. 10f) is also more complex than that seen in the preceding $L = 20$ km case (see Fig. 9d). The general structure of the normal strain rates is similar to previous experiments, but here the persistence of a band of shear (Fig. 10h) above the slippery spot at intermediate depths prevents the establishment of a vertical block of flow dominated by normal stresses. The shear profile above the sticky spot is also much weaker in the upper layers. Accordingly, λ_S reveals a band of unevenly shear-dominated deformation which is continuous across the periodic domain. Once again, shear dominated spikes extend towards the surface in association with the vanishing of the normal strain rates.

The spatial variations in the viscosity ratio (Fig. 10e) depart significantly from those of λ_S, reflecting more strikingly than for $L = 20$ km (Fig. 8e) the combined influence of the pattern of enhancement (controlled by $E(\lambda_S)$) and the effect of different strain rates, with values both above and below the range (1.0-1.39) directly controlled by $E(\lambda_S)/E_G$.

6 Discussion

In this study we conducted various ice flow simulations, comparing ESTAR with the isotropic Glen flow relation. ESTAR incorporates the observed differences between tertiary deformation rates for shear dominated and normal stress dominated stress regimes.

Our simulations of embayed ice shelf flow showed that no single Glen enhancement factor (E_G) can reproduce the anisotropic flow characteristic of the various stress regimes encountered. Significantly, while a choice of $E_G = E_S$ was necessary to reproduce the same overall velocities and ice thicknesses, which are largely controlled by lateral shear, this overestimated velocities near the ice front by up to 17% compared to ESTAR. This is a consequence of softer ice in the Glen case for the zone near the ice front, where extensional longitudinal stresses dominate. The steady-state Glen ice shelf was accordingly up to 20% thinner than the ESTAR ice shelf in this region. Even with this thinner ice influencing the ocean pressure boundary condition at the ice front, the softer ice in the Glen case meant that the longitudinal strain rates there were higher.

These results highlight one of the key failures of the Glen flow relation: an inability to account for complex, spatially varying stress regimes in its prescription of ice flow. The addition of an enhancement factor E_G to the Glen flow relation permits some compensation for the flow enhancement associated with microstructural development (i.e., rescaling the minimum creep rate data conventionally used in prescribing the Glen flow relation, e.g., Table 3.3, Cuffey and Paterson, 2010). However, such a modification does nothing to allow for the anisotropic (stress configuration dependent) aspects of ice rheology that are characteristic of tertiary creep. The improvement offered by ESTAR is that the specification of the pattern and degree of enhancement is physically based, varying spatially as a function of the stress configuration. This is achieved without the complication of a detailed treatment of microstructural information.

The ISMIP-HOM experiments B and D simulated scenarios in which the dominant control of flow was bed-parallel simple shear. In the prognostic runs with the larger aspect ratio ($L = 20$ km), only small differences were apparent between the Glen and ESTAR velocities ($< 6\%$ for ISMIPB and $< 1\%$ for ISMIPD), again provided the Glen enhancement factor was chosen equal to the ESTAR shear enhancement factor ($E_G = E_S$).

For more rapidly varying bed topography in ISMIPB, with $L = 5$ km, the differences in velocity for the two flow relations reached 25%, with surface variations of 11%. For ISMIPD, which explored variations in basal friction, the $L = 5$ km experiments still showed $< 1\%$ differences in velocities with very low strain rates, so that although a complex pattern of deformation regimes emerged, there was little effect on flow from the choice of flow relation.

These results suggest if major bed topography only varied on scales much longer than the ice thickness, close agreement between ESTAR and the Glen flow relation might be achieved more generally by choosing the tertiary shear enhancement factor as the Glen enhancement factor ($E_G = E_S$). This might provide a physical rationale to replace the *ad hoc* enhancement factors typically used in large-scale grounded ice sheet modelling with the value appropriate to flow dominated by simple shear. However, larger differences between velocities and vertical shear profiles emerged for the more rapid bedrock variation, where the importance of including longitudinal stresses in the momentum balance is already recognised (Pattyn et al., 2008), suggesting that adopting ESTAR would be preferable.

Our idealised test cases also provide some insights into the validity of the tertiary flow assumption underlying ESTAR, and the development of anisotropic crystal fabrics compatible with the current deformation regime. In the embayed ice shelf test the most significant change in the deformation regime is clearly the transition to extensive flow on approach to the ice shelf front. The contours of λ_S here are relatively well aligned with the ice flow so that flowing ice experiences gradual changes in stress regime, and the magnitudes of strain rates (e.g., Fig. 4b) and velocities (Fig. 3) indicate that in the region near the ice front,

where the Glen and ESTAR results vary appreciably, a progression of essentially compatible fabrics would be maintained. Indeed, under the prevailing deformation and flow conditions these would even develop from random fabrics over a few km.

The ISMIP-HOM experiments reveal potential violations of the tertiary flow assumption, although the significance for the flow field of these apparent short-comings needs to be assessed with regard to the somewhat artificial nature of the tests. Indeed as we saw, the difference between the ESTAR predictions and the Glen flow relations (provided $E_G = E_S$) was small, except for ISMIPB with $L = 5$ km, although of course ESTAR makes no claim to correctly describe the transient rheology of ice with an evolving anisotropy.

The ISMIP experiments have a spatial periodicity, which could allow one portion of the repetitive basal conditions to dominate the overall flow. Also, there is no surface mass budget in these experiments so that, as remarked earlier, the ice surface is a flow line, whereas in a system with surface accumulation fresh snow is always being added and advected down into the ice sheet where it makes the transition to solid ice. Accordingly, in the flow regime of these prognostic experiments even the surface layers would be regarded as having developed some anisotropy just as the lower layers would, since they have in principle been deforming over an arbitrarily long time.

The main issue about the establishment of tertiary flow conditions in the periodic environment of our ISMIP experiments concerns the possible cycling of the flowing ice through a variety of stress regimes. This leads to transition regions where the stress regime and presumably the crystal anisotropy would be evolving, and the compatibility assumptions behind ESTAR could locally be violated. Clearly the spatial extent of transitional flow and the delay in attaining any new tertiary state depends on the magnitudes of the strain rates and the velocity of the ice. By combining these with a threshold for accumulated strain as the criterion for development of a compatible (tertiary) fabric under a persistent flow regime, the extent of a transition zone can be estimated. This scale can then be compared to the horizontal variation of the stress regime. Selecting the 10% strain required to develop a compatible anisotropy from initially randomly oriented ice should provide a conservative yardstick, when applied to gradual changes in stress regime.

The patterns of stress regimes revealed by the distributions of λ_S (Figs. 6d, 7d, 9a, and 10f) indicate where along-flow variations in stress regime might be too rapid to sustain the assumption that a compatible crystallographic anisotropy had evolved. For the ISMIPB experiments this concern is essentially focussed to the near surface spikes in λ_S around the two locations where longitudinal deformations vanish, since the anisotropy of deeper ice will be compatible with deformation dominated by simple shear. There may be some complications with a slow cycling of the upper levels between extensive and compressive flow. Very near the surface, the λ_S peak intervals are narrow and the shear strain rates there are very small (corresponding to transition scales of several kilometres) so that there will be no appreciable development of a shear compatible fabric. Either side of the peaks, the main extensive and compressive flow domains for $L = 20$ km (see Fig. 6e) are ≈ 5 km long and have transition scales of < 1 km which suggests that the strongly normal stress dominated upper layer will be mainly in tertiary state. Turning to the transient shear intrusions into this layer: at 100 m depth over the bump the shear transition scale is 3 km while at 200 m depth over the depression the shear transition scale is ≈ 5 km, suggesting that that the λ_S peaks do represent a local failure of ESTAR's tertiary assumption. Throughout the domain the lower half of the ice column has transition

scales of ≤ 300 m which, given the gradual variations in λ_S and the direction of ice flow, indicates that region is in the tertiary state.

For ISMIPB with $L = 5$ km, which displays a generally deeper band of normal stress dominated regime (Fig. 7d), the transition scales for the compressive and extensive regions are ~ 500 m for regions of ≈ 1 km in extent, while the shear transition scales at 100 m depth above the bump and 200 m depth above the depression are now ~ 10 km and ~ 1 km, respectively. For most of the domain the transition rates in the lower half of the ice column are ≤ 100 m, although this rises to nearly 1000 m above the bedrock bump.

In the ISMIPD case, for $L = 20$ km, the pattern of λ_S (Fig. 9a) shows there are also transitions between simple shear dominated and extension dominated deformation associated with the slippery region, with varying abruptness at different depths, and some of the contours of λ_S in this instance almost orthogonal to the ice flow. A complication is that there is very little longitudinal deformation (Fig. 9e) occurring over the slippery region because the overall flow is controlled by the periodic sticky spot. Accordingly, there would not be any significant fabric evolution across this ~ 4 km region (estimated transition scales there are > 40 km) so that the tertiary assumption and using E_C (since $\lambda_S = 1$) would be inappropriate. Once again, the low strain rates here (Figs. 9e-f) translate into very stiff ice and might make the influence of ESTAR enhancement factors relatively unimportant. A factor of 100 in $\dot{\varepsilon}_e$ changes viscosity by a factor of 21.5, whereas the maximum viscosity contrast from $E(\lambda_S)$ is 1.39. The shear strain rates are also very low, with transition scales > 1 km except very close to the bed over the sticky spot. Accordingly, while a compatible fabric could be expected where the large λ_S values are shown in Fig. 6a, its presence would be due to the periodic flow, and the inability of the $\lambda_S \sim 0$ region to modify it.

For the last test, ISMIPD with $L = 5$ km, strain-rates are once again very low, and there is no simple structure to the picture of the stress regime portrayed by λ_S in Fig. 10f. Below mid-depth there is a periodically continuous band of shear that might favour the development of crystal anisotropy, but clearly the tertiary flow assumption of ESTAR would not be particularly useful here.

The focus of this study was to explore the effect on the dynamic response of ice sheets of using an anisotropic (ESTAR) description of rheology, sensitive to the varying proportions of simple shear and normal stresses, compared to using the standard (Glen) isotropic description of rheology. Our results, particularly with respect to the differences between the Glen and ESTAR simulations, are sensitive to the choice of E_S and E_C. Experimental evidence (Treverrow et al., 2012) suggests that the ratio $E_S/E_C = 8/3$, rather than their overall magnitude, is the dominant control in the level of enhancement $E(\lambda_S)$ and corresponding dynamic response of grounded and floating ice sheets. Here, we used values of $E_S = 8$ and $E_C = 3$, which are based on laboratory experiments of tertiary creep (Treverrow et al., 2012), and which yield values for the overall enhancement that are compatible with estimates from borehole inclination measurements (e.g., Russell-Head and Budd, 1979) and modelling studies (e.g., Wang and Warner, 1999). Nevertheless, further investigation into suitable values of E_S and E_C to use in numerical modelling studies of grounded and floating ice sheets is warranted. Indeed, with the implementation of ESTAR in ISSM, it might be possible to use inverse methods to infer values of E_S and E_C that improved the match between modelled and observed surface velocities.

In order to examine the impact of an anisotropic rheology on simulated ice dynamics, the ISMIP-HOM and embayed ice shelf experiments were carried out assuming isothermal conditions. However, as discussed earlier, real ice sheets and ice shelves typically have cold, upper layers and strong vertical gradients in temperature, and these will often be stronger controls on vertical contrasts in deformation rates, through $A(T')$ (Eqs. 2-3), than a factor of 3 to 8 produced by anisotropic enhancement.

7 Conclusions

We have investigated some consequences of incorporating the flow properties of anisotropic ice into modelling flow in ice sheets and ice shelves. Specifically, we have investigated the flow response to prolonged deformation under a constant or slowly changing stress regime and the associated development of an anisotropic crystal orientation fabric compatible with that deformation, as represented by the empirical, scalar, tertiary, anisotropic rheology of Budd et al. (2013) – ESTAR. Having implemented this rheology in ISSM, we made initial studies in the context of idealised experiments: for an embayed ice shelf, and in two-dimensional models of grounded ice flow over varying topography and variable basal friction previously explored by ice flow modellers (Pattyn et al., 2007, 2008). We have demonstrated that ESTAR is a computationally-efficient anisotropic rheology for large-scale ice sheet models. We have highlighted that ESTAR produces different flow responses compared with the prevailing rheological description based on the Glen flow relation, in regions where simple shear and normal stresses, and combinations of these, are drivers of ice flow. We have also noted some possible limitations of this empirical treatment of the tertiary flow regime, although their significance and whether there is scope for developing the empirical approach to resolve them remain to be determined. It would also be interesting to compare ESTAR with the predictions of modelling that uses more complex rheological descriptions, even if the comparison was limited to local domains or idealised cases.

Our embayed ice shelf results have significant implications for ice sheet model simulations that rely on the Glen flow relation to simulate past, present, and future ice flow, which are used to constrain uncertainty in reconstructions and projections of sea levels. In particular, the effect of unrealistically fast thinning ice near the calving front, as simulated with the Glen flow relation, is to deform the ice shelf, which could lead to unrealistic ice shelf geometries and affect buttressing if it were to spread beyond the "passive ice" sector (Furst et al., 2016) near the ice front.

With the implementation of ESTAR into ISSM completed, further investigation into the capabilities of ESTAR to replicate real-world ice sheet flow in Antarctic outlet glaciers is currently underway.

Code availability. The results from this work are reproducible using ISSM (from version 4.11). The current version of ISSM is available for download at https://issm.jpl.nasa.gov. The ISMIP-HOM experiments are documented in Pattyn et al. (2007).

Competing interests. The authors have no competing interests.

Acknowledgements. The authors thank two anonymous reviewers for their comments that resulted in an improved manuscript. This work was supported under the Australian Research Council's Special Research Initiative for Antarctic Gateway Partnership (Project ID SR140300001), and the Australian Government's Cooperative Research Centres Programme through the Antarctic Climate and Ecosystems Cooperative Research Centre (ACE CRC). The University of Tasmania supported the visit of MM to Hobart. This research was undertaken with the assistance of resources from the National Computational Infrastructure (NCI), which is supported by the Australian Government.

References

Azuma, N. and Goto-Azuma, K.: An anisotropic flow law for ice sheet ice and its implications, Ann. Glaciol., 23, 202–208, 1996.

Blatter, H.: Velocity And Stress-Fields In Grounded Glaciers: A Simple Algorithm For Including Deviatoric Stress Gradients, J. Glaciol., 41, 333–344, 1995.

Breuer, B., Lange, M. A., and Blindow, N.: Sensitivity studies on model modifications to assess the dynamics of a temperature ice cap, such as that on King George Island, Antarctica, J. Glaciol., 52, 235–247, 2006.

Budd, W. and Jacka, T.: A review of ice rheology for ice sheet modelling, Cold Reg. Sci. Technol., 16, 107–144, 1989.

Budd, W. F.: The development of crystal orientation fabrics in moving ice, Z. Gletscherkd. Glazialgeol, 8, 65–105, 1972.

Budd, W. F., Warner, R. C., Jacka, T. H., Li, J., and Treverrow, A.: Ice flow relations for stress and strain-rate components from combined shear and compression laboratory experiments, J. Glaciol., 59, 374–392, doi:10.3189/2013JoG12J106, 2013.

Cuffey, K. and Paterson, W. S. B.: The Physics of Glaciers, 4th Edition, Elsevier, Oxford, 2010.

DiPrinzio, C., Wilen, L., Alley, R., Fitzpatrick, J., Spencer, M., and Gow, A.: Fabric and texture at Siple Dome, Antarctica, J. Glaciol., 51, 281–290, 2005.

Durand, G., Gagliardini, O., Zwinger, T., Le Meur, E., and Hindmarsh, R.: Full Stokes modeling of marine ice sheets: influence of the grid size, Ann. Glaciol., 50, 109–114, 2009.

Duval, P.: Creep and fabrics of polycrystalline ice under shear and compression, J. Glaciol., 27, 129–140, 1981.

Ern, A. and Guermond, J.-L.: Applied Mathematical Sciences, vol. 159, chap. Theory and practice of finite elements, pp. 175–217, Springer, 2004.

Faria, S. H., Weikusat, I., and Azuma, N.: The microstructure of polar ice. Part II: State of the art, J. Struct. Geol., 61, 21 – 49, doi:10.1016/j.jsg.2013.11.003, 2014.

Furst, J. J., Durand, G., Gillet-Chaulet, F., Tavard, L., Rankl, M., Braun, M., and Gagliardini, O.: The safety band of Antarctic ice shelves, Nat. Clim. Change, 6, 479–482, doi:10.1038/NCLIMATE2912, 2016.

Gagliardini, O., Gillet-Chaulet, F., and Montagnat, M.: A review of anisotropic polar ice models: from crystal to ice-sheet flow models, in: Physics of Ice Core Records II, edited by Hondoh, T., pp. 149–166, Institute of Low Temperature Science, Hokkaido University, Sapporo, Japan, 2009.

Gao, X. and Jacka, T.: The approach to similar tertiary creep rates for Antarctic core ice and laboratory prepared ice, Journal de Physique, Colloque C1, supplement to no. 3, Tome 48, pp. 289–296, 1987.

Gillet-Chaulet, F., Gagliardini, O., Meyssonnier, J., Montagnat, M., and Castelnau, O.: A user-friendly anisotropic flow law for ice-sheet modelling, J. Glaciol., 51, 3–14, doi:10.3189/172756505781829584, 2005.

Glen, J.: The creep of polycrystalline ice, Proc. R. Soc. A, 228, 519–538, 1955.

Glen, J.: The flow law of ice: A discussion of the assumptions made in glacier theory, their experimental foundations and consequences, IASH Publ, 47, 171–183, 1958.

Glen, J. W.: Experiments on the deformation of ice, J. Glaciol., 2, 111–114, 1952.

Glen, J. W.: Rate of flow of polycrystalline ice, Nature, 172, 721–722, 1953.

Gödert, G.: A mesocopic approach for modelling texture evolution of polar ice including recrystallisation phenomena, Ann. Glaciol., 37, 23–28, doi:10.3189/172756403781815375, 2003.

Greve, R.: Relation of measured basal temperatures and the spatial distribution of the geothermal heat flux for the Greenland ice sheet, Ann. Glaciol., 42, 424–432, 2005.

Greve, R. and Blatter, H.: Dynamics of Ice Sheets and Glaciers, Advances in Geophysical and Environmental Mechanics and Mathematics, Springer-Verlag, 2009.

Greve, R. and Blatter, H.: Comparison of thermodynamics solvers in the polythermal ice sheet model SICOPOLIS, Polar Science, 10, 11 – 23, doi:http://dx.doi.org/10.1016/j.polar.2015.12.004, 2016.

Hulbe, C. L., Wang, W., Joughin, I. R., and Siegert, M. J.: The role of lateral and vertical shear in tributary flow toward a West Antarctic ice stream, Ann. Glaciol., 36, 244–250, 2003.

Huybrechts, P., Rybak, O., Pattyn, F., Ruth, U., and Steinhage, D.: Ice thinning, upstream advection, and non-climatic biases for the upper 89% of the EDML ice core from a nested model of the Antarctic ice sheet, Clim. Past, 3, 577–589, 2007.

Jacka, T. and Maccagnan, M.: Ice crystallographic and strain rate changes with strain in compression and extension, Cold Reg. Sci. Technol., 8, 269–286, 1984.

Jaeger, J. C.: Elasticity, fracture and flow: with engineering and geological applications, Methuen, 3rd edn., 1969.

Kamb, B.: Experimental recrystallization of ice under stress, American Geophysical Union, 1973.

Kipfstuhl, S., Faria, S., Azuma, N., Freitag, J., Hamann, I., Kaufmann, P., Miller, H., Weiler, K., and Wilhelms, F.: Evidence of dynamic recrystallization in polar firn, J. Geophys. Res., 114, B05 204, 2009.

Larour, E., Seroussi, H., Morlighem, M., and Rignot, E.: Continental scale, high order, high spatial resolution, ice sheet modeling using the Ice Sheet System Model (ISSM), J. Geophys. Res., 117, 1–20, doi:10.1029/2011JF002140, 2012.

Li, J. and Jacka, T.: Correspondence. Horizontal shear rate of ice initially exhibiting vertical compression fabrics, J. Glaciol., 44, 670–672, 1998.

Li, J., Jacka, J., and Budd, W. F.: Deformation rates in combined compression and shear for ice which is initially isotropic and after the development of strong anisotropy, Ann. Glaciol., 23, 247–252, 1996.

Lile, R.: The effect of anisotropy on the creep of polycrystalline ice, J. Glaciol., 21, 475–483, 1978.

Lliboutry, L.: Anisotropic, transversely isotropic nonlinear viscosity of rock ice and rheological parameters inferred from homogenization, Int. J. Plasticity, 9, 619–632, 1993.

Ma, Y., Gagliardini, O., Ritz, C., Gillet-Chaulet, F., Durand, G., and Montagnat, M.: Enhancement factors for grounded ice and ice shelves inferred from an anisotropic ice-flow model, J. Glaciol., 56, 805–812, 2010.

MacAyeal, D.: Large-scale ice flow over a viscous basal sediment: Theory and application to Ice Stream B, Antarctica, J. Geophys. Res., 94, 4071–4087, 1989.

Martín, C. and Gudmundsson, G. H.: Effects of nonlinear rheology, temperature and anisotropy on the relationship between age and depth at ice divides, The Cryosphere, 6, 1221–1229, doi:10.5194/tc-6-1221-2012, 2012.

Montagnat, M., Azuma, N., Dahl-Jensen, D., Eichler, J., Fujita, S., Gillet-Chaulet, F., Kipfstuhl, S., Samyn, D., Svensson, A., and Weikusat, I.: Fabric along the NEEM ice core, Greenland, and its comparison with GRIP and NGRIP ice cores, The Cryosphere, 8, 1129–1138, doi:10.5194/tc-8-1129-2014, 2014.

Morgan, V., Wookey, C., Li, J., van Ommen, T., Skinner, W., and Fitzpatrick, M.: Site information and initial results from deep ice drilling on Law Dome, Antarctica, J. Glaciol., 43, 3–10, 1997.

Morgan, V., van Ommen, T., Elcheikh, A., and Li, J.: Variations in shear deformation rate with depth at Dome Summit South, Law Dome, East Antarctica, Ann. Glaciol., pp. 135–139, 1998.

Nye, J. F.: The flow law of ice from measurements in glacier tunnels, laboratory experiments and the Jungfraufirn borehole experiment, Proc. R. Soc. A, 219, 477–489, 1953.

Paterson, W.: The Physics of Glaciers, Pergamon Press, Oxford, London, New York, 3rd edn., 1994.

Pattyn, F.: A new three-dimensional higher-order thermomechanical ice sheet model: Basic sensitivity, ice stream development, and ice flow across subglacial lakes, J. Geophys. Res., 108, 1–15, doi:10.1029/2002JB002329, 2003.

Pattyn, F., Perichon, L., Aschwanden, A., Breuer, B., De Smedt, B., Gagliardini, O., Hindmarsh, R., Hubbard, A., Johnson, J., Kleiner, T., Konovalov, Y., Martin, C., Payne, T., Pollard, D., Price, S., Saito, F., and Sugiyama, S.: ISMIP-HOM: Results of the Higher-Order Ice Sheet Model Intercomparison Project, in: European Geosciences Union, 2007.

Pattyn, F., Perichon, L., Aschwanden, A., Breuer, B., de Smedt, B., Gagliardini, O., Gudmundsson, G. H., Hindmarsh, R. C. A., Hubbard, A., Johnson, J. V., Kleiner, T., Konovalov, Y., Martin, C., Payne, A. J., Pollard, D., Price, S., Rückamp, M., Saito, F., Soucek, O., Sugiyama, S., and Zwinger, T.: Benchmark experiments for higher-order and full-Stokes ice sheet models (ISMIP-HOM), The Cryosphere, 2, 95–108, 2008.

Pettit, E., Thorsteinsson, T., Jacobson, H., and Waddington, E.: The role of crystal fabric in flow near an ice divide, J. Glaciol., 53, 277–288, doi:10.3189/172756507782202766, 2007.

Pimienta, P., Duval, P., and Lipenkov, V. Y.: Mechanical behaviour of anisotropic polar ice, in: The Physical Basis of Ice Sheet Modelling, pp. 57–65, IAHS Publ. 170, 1987.

Placidi, L., Greve, R., Seddik, H., and Faria, S.: Continuum-mechanical, Anisotropic Flow model, for polar ice masses, based on an anisotropic Flow Enhancement factor, Continuum Mech. Thermodyn., 22, 221–237, doi:10.1007/s00161-009-0126-0, 2010.

Russell-Head, D. and Budd, W.: Ice-sheet flow properties derived from bore-hole shear measurements combined with ice-core studies, J. Glaciol., 24, 117–130, 1979.

Saito, F. and Abe-Ouchi, A.: Thermal structure of Dome Fuji and east Dronning Maud Land, Antarctica, simulated by a three-dimensional ice-sheet model, in: Ann. Glaciol., VOL 39, edited by Jacka, J, vol. 39 of *Ann. Glaciol.*, INT GLACIOLOGICAL SOC, LENSFIELD RD, CAMBRIDGE CB2 1ER, ENGLAND, 2004.

Schmid, E. and Boas, W.: Plasticity of crystals, F.A. Hughes and Co. Ltd., London, 1950.

Seddik, H., Greve, R., Zwinger, T., and Placidi, L.: A full Stokes ice flow model for the vicinity of Dome Fuji, Antarctica, with induced anisotropy and fabric evolution, The Cryosphere, 5, 495–508, doi:10.5194/tc-5-495-2011, 2011.

Staroszczyk, R. and Gagliardini, O.: Two orthotropic models for strain-induced anisotropy of polar ice, J. Glaciol., 45, 485–494, 1999.

Thorsteinsson, T.: An analytical approach to deformation of anisotropic ice-crystal aggregates, J. Glaciol., 47, 507–516, 2001.

Thorsteinsson, T.: Fabric development with nearest-neighbour interaction and dynamic recrystallization, J. Geophys. Res. - Solid Earth, 107, doi:10.1029/2001JB000244, 2002.

Treverrow, A., Budd, W. F., Jacka, T. H., and Warner, R. C.: The tertiary creep of polycrystalline ice: experimental evidence for stress-dependent levels of strain-rate enhancement, J. Glaciol., 58, 301–314, doi:10.3189/2012JoG11J149, 2012.

Treverrow, A., Warner, R. C., Budd, W. F., Jacka, T. H., and Roberts, J. L.: Modelled stress distributions at the Dome Summit South borehole, Law Dome, East Antarctica: a comparison of anisotropic ice flow relations, J. Glaciol., 61, 987–1004, doi:13.3189/2016JoG14J198, 2015.

Treverrow, A., Jun, L., and Jacka, T. H.: Ice crystal c-axis orientation and mean grain size measurements from the Dome Summit South ice core, Law Dome, East Antarctica, Earth System Science Data, 8, 253–263, doi:10.5194/essd-8-253-2016, 2016.

Trickett, Y., Baker, I., and Pradhan, P.: The orientation dependence of the strength of ice single crystals, J. Glaciol., 46, 41–44, doi:10.3189/172756500781833296, 2000.

van der Veen, C. J. and Whillans, I. M.: Force budget: I. Theory and numerical methods, J. Glaciol., 35, 53–60, 1989.

van der Veen, C. J. and Whillans, I. M.: Development of fabric in ice, Cold Reg. Sci. Technol., pp. 171–195, doi:10.1016/0165-232X(94)90027-2, 1994.

Wang, W. and Warner, R. C.: Modelling of anisotropic ice flow in Law Dome, East Antarctica, Ann. Glaciol., 29, 184–190, 1999.

Wang, W., Warner, R. C., and Budd, W. F.: Ice-flow properties at Dome Summit South, Law Dome, East Antarctica, Ann. Glaciol., 35, 567–573, 2002a.

Wang, W., Jun, L., Zwally, H. J., Morgan, V., and van Ommen, T. D.: The effect of anistropic flow properties on ice-sheet surface elevation change, Ann. Glaciol., 39, 439–444, 2004.

Wang, W., Li, J., and Zwally, H. J.: Dynamic inland propagation of thinning due to ice loss at the margins of the Greenland ice sheet, J. Glaciol., 58, 734–740, doi:10.3189/2012JoG11J187, 2012.

Wang, W. L. and Warner, R. C.: Simulation of the influence of ice rheology on velocity profiles and ice-sheet mass balance, Ann. Glaciol., 27, 194–200, 1998.

Wang, W. L., Zwally, H. J., Abdalati, W., and Luo, S.: Modeling of ice flow and internal layers along a flowline through Swiss Camp, West Greenland, Ann. Glaciol., 34, 303–308, 2002b.

Wang, W. L., Zwally, H. J., Hulbe, C. L., Siegert, M. J., and Joughin, I. R.: Anisotropic ice flow leading to the onset of Ice Stream D, West Antarctica: numerical modelling based on the observations from Byrd Station borehole, Ann. Glaciol., 37, 397–403, 2003.

Warner, R. C., Jacka, T. H., Li, J., and Budd, W. F.: Tertiary flow relations for compression and shear components in combined stress tests on ice, in: Advances in cold-region thermal engineering and sciences: technological, environmental, and climatological impact, edited by Hutter, K., Wang, Y., and Beer, H., pp. 259–270, Springer-Verlag, 1999.

Weertman, J.: Deformation of floating ice shelves, J. Glaciol., 3, 38–42, 1957.

Winkelmann, R., Martin, M. A., Haseloff, M., Albrecht, T., Bueler, E., Khroulev, C., and Levermann, A.: The Potsdam Parallel Ice Sheet Model (PISM-PIK) - Part 1: Model description, The Cryosphere, 5, 715–726, doi:10.5194/tc-5-715-2011, 2011.

Zwinger, T., Schäfer, M., Martín, C., and Moore, J. C.: Influence of anisotropy on velocity and age distribution at Scharffenbergbotnen blue ice area, The Cryosphere, 8, 607–621, doi:10.5194/tc-8-607-2014, 2014.

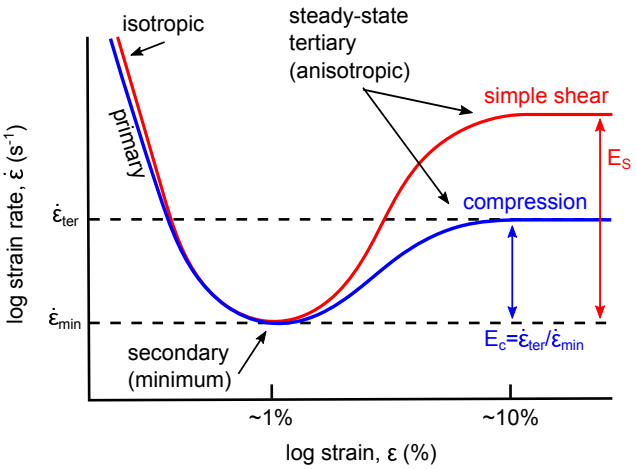

Figure 1. Strain rate characteristics of polycrystalline ice undergoing deformation driven by single stresses as measured in laboratory experiments. The part of the curve corresponding to tertiary (steady-state) anisotropic creep is relevant to the deformation of ice masses in typical ice sheets and glaciers. The red (blue) curve illustrates the result of simple shear-alone (compression-alone) stress configurations. Note that the ratio of the shear enhancement factor E_S to the compression enhancement factor E_C is approximately $8/3$, and the enhancement due to compression-alone is approximately three times that of the secondary (minimum) creep rate.

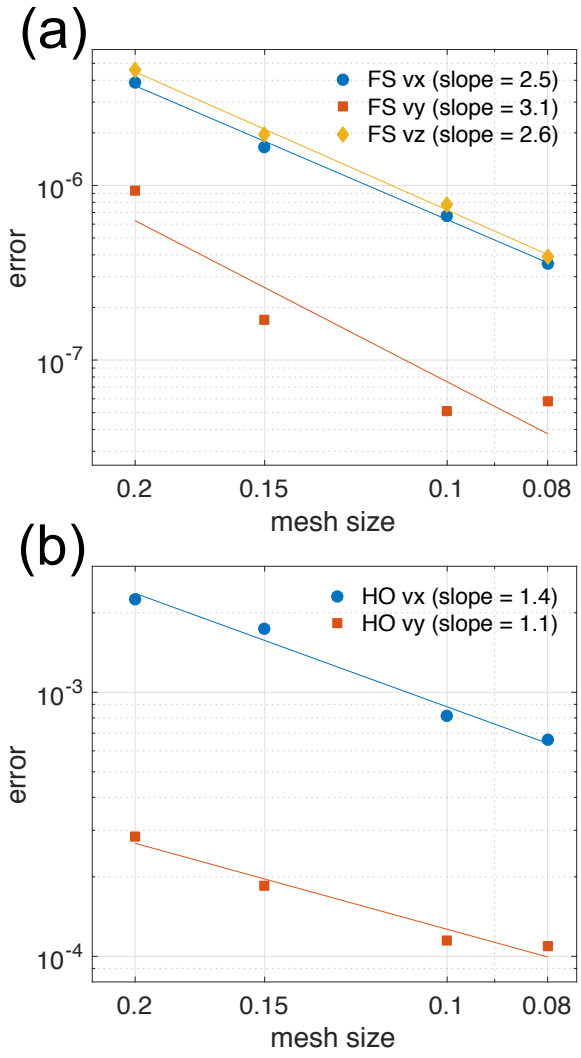

Figure 2. Convergence rates of the simulated **(a)** full-Stokes (FS) and **(b)** higher-order (HO) velocity fields (v_x, v_y, v_z) to the analytical solutions in Eqs. 13-17 for increasing mesh resolutions.

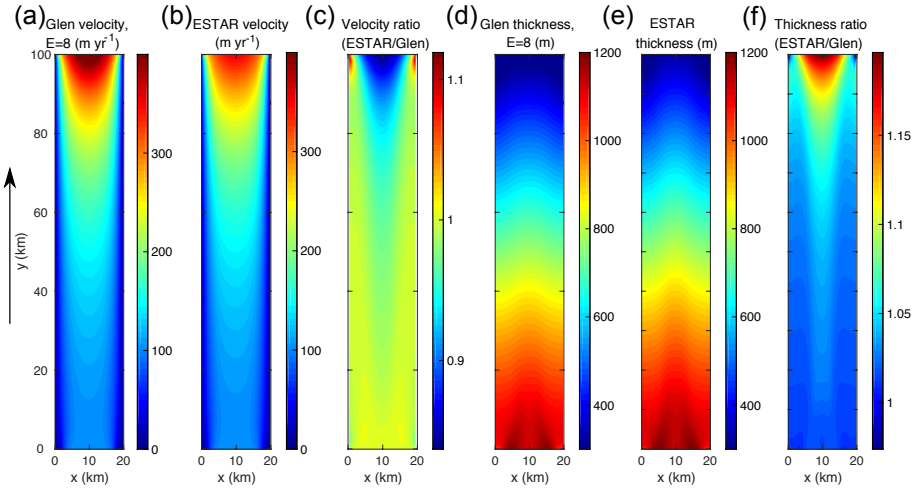

Figure 3. Rectangular ice shelf HO steady-state surface fields. **(a)** Velocity magnitude (m yr^{-1}) for the Glen flow relation ($E_G = 8$); **(b)** velocity magnitude (m yr^{-1}) for ESTAR; **(c)** ratios (i.e., ESTAR/Glen) of velocity magnitudes; **(d)** thickness (m) for the Glen flow relation ($E_G = 8$); **(e)** thickness (m) for ESTAR; and **(f)** ratios (i.e., ESTAR/Glen) thicknesses. The black arrow indicates the direction of flow.

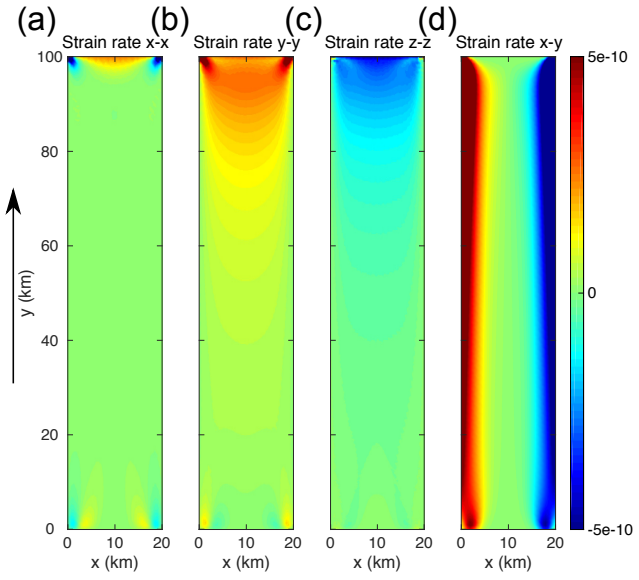

Figure 4. Rectangular ice shelf ESTAR HO steady-state surface strain rates (s^{-1}): **(a)** $\dot{\varepsilon}_{xx}$; **(b)** $\dot{\varepsilon}_{yy}$, **(c)** $\dot{\varepsilon}_{zz}$; and **(d)** $\dot{\varepsilon}_{xy}$.

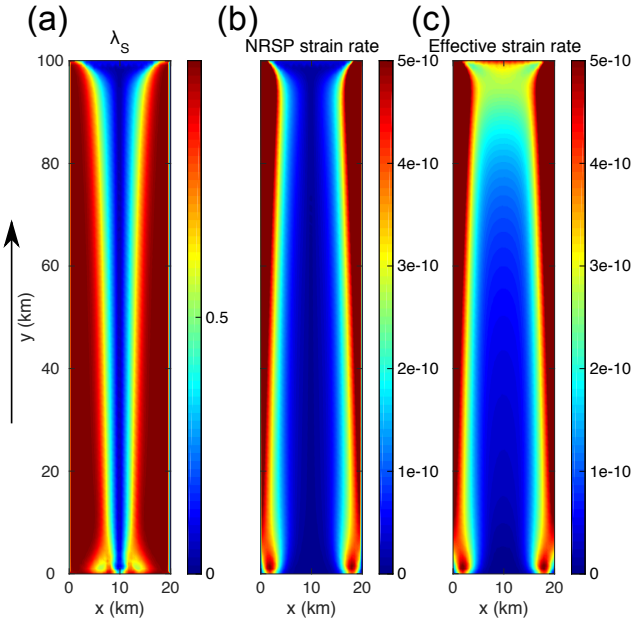

Figure 5. Rectangular ice shelf ESTAR HO steady-state surface fields. **(a)** ESTAR shear ratio λ_S; **(b)** shear strain rate resolved on the non-rotating shear plane (NRSP) $\dot{\varepsilon}'$ (s^{-1}); and **(c)** effective strain rate $\dot{\varepsilon}_e$ (s^{-1}). The black arrow indicates the direction of flow.

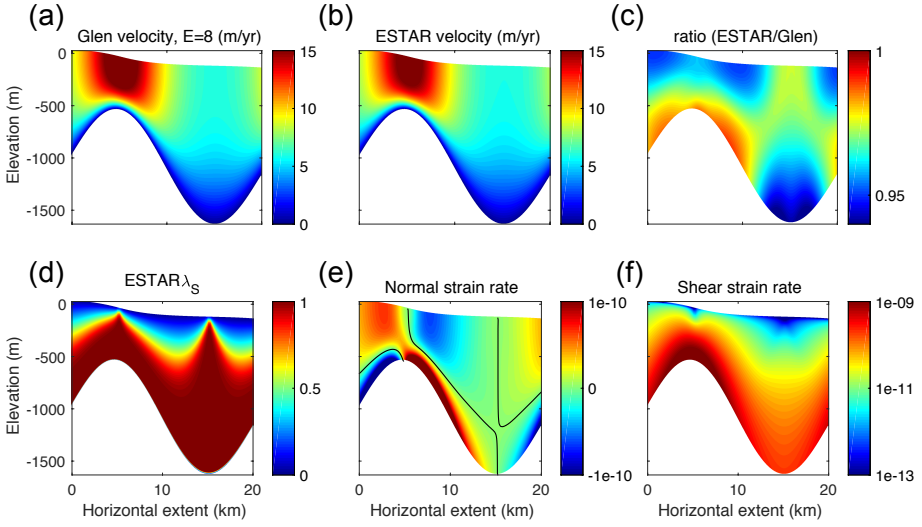

Figure 6. ISMIPB FS steady-state results with horizontal extent $L = 20$ km. **(a)** Horizontal velocity v_x (m yr^{-1}) for the Glen flow relation with $E_G = 8$; **(b)** v_x (m yr^{-1}) for ESTAR with $E_S = 8$ and $E_C = 3$; and **(c)** ratio between the Glen and ESTAR v_x fields; **(d)** ESTAR shear enhancement factor λ_S (Eq. 6); **(e)** ESTAR normal strain rate (i.e., $x - x$ strain rate; s^{-1}); and **(f)** ESTAR shear strain rate (i.e., $x - z$ strain rate; s^{-1}). The black contours in **(e)** correspond to the curves where $\dot{\epsilon}_{xx} = 0$. Note the log scale in **(f)**.

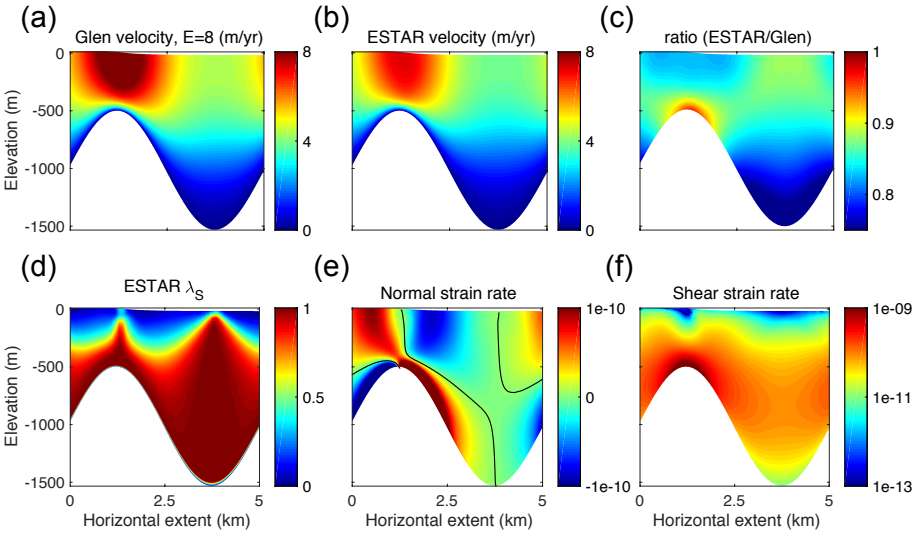

Figure 7. ISMIPB FS steady-state results with horizontal extent $L = 5$ km. **(a)** Horizontal velocity v_x (m yr^{-1}) for the Glen flow relation with $E_G = 8$; **(b)** v_x (m yr^{-1}) for ESTAR with $E_S = 8$ and $E_C = 3$; and **(c)** ratio between the Glen and ESTAR v_x fields; **(d)** ESTAR shear enhancement factor λ_S (Eq. 6); **(e)** ESTAR normal strain rate (i.e., $x - x$ strain rate; s^{-1}); and **(f)** ESTAR shear strain rate (i.e., $x - z$ strain rate; s^{-1}). The black contours in **(e)** correspond to the curves where $\dot{\epsilon}_{xx} = 0$. Note the log scale in **(f)**.

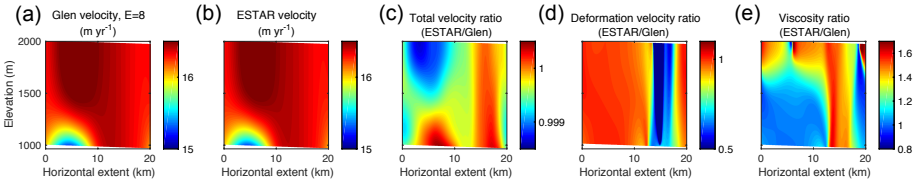

Figure 8. ISMIPD FS steady-state results with horizontal extent $L = 20$ km. **(a)** Glen horizontal velocities v_x (m yr^{-1}); **(b)** ESTAR v_x (m yr^{-1}); **(c)** ratios of ESTAR/Glen v_x; **(d)** ratios of ESTAR/Glen deformation velocities (i.e., the difference between v_x and the sliding velocity, which is taken to be equal to the velocity along the basal mesh points); and **(e)** ratios of ESTAR/Glen viscosities.

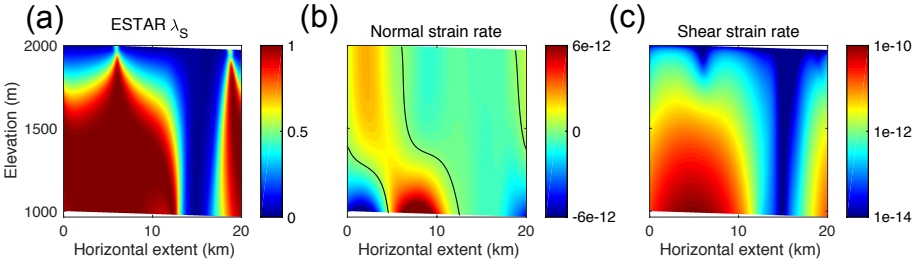

Figure 9. ISMIPD ESTAR FS steady-state enhancement factors and normal and shear strain rates with horizontal extent $L = 20$ km. **(a)** λ_S; **(b)** normal strain rates (s^{-1}); and **(c)** shear strain rates (s^{-1}). The black contour lines in **(b)** correspond to the curves where $\dot{\epsilon}_{xx} = 0$. Note the log scale in **(c)**.

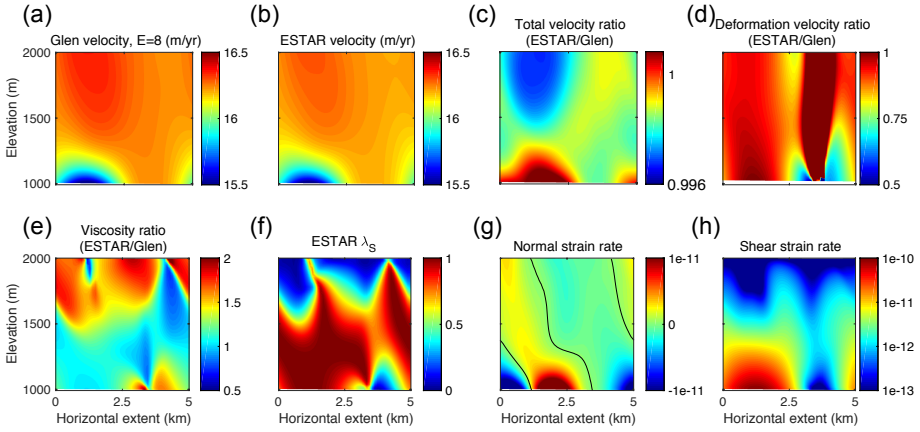

Figure 10. ISMIPD FS steady-state results with horizontal extent $L = 5$ km. **(a)** Glen horizontal velocity v_x (m yr^{-1}, with $E_G = 8$); **(b)** ESTAR v_x (m yr^{-1}); **(c)** ratio of ESTAR/Glen v_x; **(d)** ratio of ESTAR/Glen deformation v_x; **(e)** ratio of ESTAR/Glen viscosity; **(f)** ESTAR λ_S; **(g)** ESTAR normal strain rate (s^{-1}); and **(h)** ESTAR shear strain rate (s^{-1}). The black contours in **(g)** correspond to the curves where $\dot{\varepsilon}_{xx} = 0$. Note the log scale in **(h)**.

Table 1. Computational times for full-Stokes simulations of the embayed ice shelf (Sect. 5.1) using Glen and ESTAR for increasing mesh resolution. The model is simulated for 1 month and for a total of 833 time steps in each case. Dof stands for model degrees of freedom.

Dof	Vertices	CPUs	Glen walltime (s)	ESTAR walltime (s)
2210	10040	16	9084	9281
2760	15665	32	10467	10778
3310	22540	64	12920	13008
4410	40040	128	20852	21008
8820	80080	256	59057	59934